Towards Robust River Plastic Detection: Combining Lab and Field-based Hyperspectral Imagery

Paolo Tasseron[1], Louise Schreyers[1], Joseph Peller[2], Lauren Biermann[3], and Tim van Emmerik[1]

[1]Hydrology and Quantitative Water Management Group, Wageningen University and Research, 6708 PB Wageningen, The Netherlands

[2]Plant Sciences Group, Wageningen University and Research, 6708 PB Wageningen, The Netherlands

[3]Plymouth Marine Laboratory, Prospect Place, Plymouth PL1 3DH, UK

Abstract

Plastic pollution in aquatic ecosystems has increased dramatically in the last five decades, with strong impacts on human and aquatic life. Recent studies endorse the need for innovative approaches to monitor the presence, abundance, and types of plastic in these ecosystems. One approach gaining rapid traction is the use of multi- and hyperspectral cameras. However, most experiments using this approach have been conducted in controlled environments, making findings challenging to apply in natural environments. We present a method linking lab- and field-based identification of macroplastics using hyperspectral data (1150-1675 nm). Experiments using riverbank-harvested macroplastics were set up in (1) a laboratory environment, and (2) on the banks of the Rhine River. Representative pixel selections of eleven lab-based images (n = 786,264 pixels) and two field-based images (n = 40,289 pixels) were used to analyse the differences between these two environments. Next, classifier algorithms such as support vector machines (SVM), spectral angle mappers (SAM) and spectral information divergence (SID) were applied, because of their robustness to varying light conditions and high accuracies in mapping spectral similarities. Our results showed that SAM classifiers are most robust in separating plastic debris from natural or anthropogenic background elements. By applying lab-based data for plastic detection in field-based images, user accuracies for plastics to up to 93.6% (n = 8,370 plastic pixels) were attained. This study provides key fundamental insights in linking lab-based data to plastic detection in the field. With this paper we aim to contribute to the development of future spectral missions to detect and monitor plastic pollution in aquatic ecosystems.

Keywords: classification, hyperspectral, reflectance, macrolitter, spectral angle mapping, monitoring

1 Introduction

Plastic pollution in aquatic ecosystems has increased drastically in the last decades, with strong impacts on human and aquatic life. Recent estimates suggest 19-23 million metric tonnes of macroplastic enter aquatic ecosystems, of which 0.8-2.7 million metric tonnes enters the oceans through rivers annually [1,2]. Therefore, there is a need for innovative approaches to monitor the presence and abundance of plastics in aquatic ecosystems [3,4]. An approach gaining rapid attention in the remote sensing community is multispectral or hyperspectral imaging of plastics. Hyperspectral imaging of plastics is key to better understand plastic-specific detection features and the subsequent design of new monitoring instruments [5, 6]. Subsequently, these techniques offer potential for upscaling and harmonization plastic monitoring across aquatic ecosystems.

Recent studies have shown plastics are characterised by unique spectral reflectance signatures in the near infrared (NIR) to shortwave infrared (SWIR) part of the electromagnetic spectrum, especially in the $1100 - 1700$ nm range. Most of the studies focused on characterising the reflection signatures in controlled environments of virgin plastics [5, 7–10], marine or riverbank-harvested plastics [11–13], or a combination of virgin plastics and harvested plastics [14–18]. Only few experiments with hyperspectral imaging systems to detect macroplastics have been performed in aquatic environments [19–21].

Therefore, it is imperative to understand how laboratory experiments or experiments in controlled environments relate to measurements in natural aquatic ecosystems. As the number of multispectral and hyperspectral reference databases and libraries is increasing (e.g. [5, 15, 16]), the potential for their usage in identification and detection of plastics in aquatic ecosystems is growing. Goddijn-Murphy and Dufaur [11] evaluated plastic identification algorithms for a field experiment and laboratory measurements. They concluded many factors such as the plastic polymer composition, transparency, shape, surface roughness and lighting conditions to affect the correlation between reflectance patterns in the field and laboratory experiments. In addition, Martínez-Vicente et al. [22] argued it is a challenge to confirm to what extent reflection characteristics observed in a laboratory can be used for detecting floating macroplastics in aquatic ecosystems.

It is currently unclear to what extent hyperspectral imaging of plastics in controlled environments is useful for detecting and identifying floating plastics in rivers and on riverbanks. Yet, the potential of multispectral and hyperspectral imaging for plastic detection is high [11,20,23]. Therefore, this study develops insights in linking lab- and field-based hyperspectral methods for identification of macroplastics. First, an assessment of the reflectance patterns in natural aquatic ecosystems is made to understand how plastic signatures behave in these environments. Second, a direct comparison with reflectance of plastics in a controlled is made to assess the differences and how these can be managed in a classifier. Lastly, an indication of the accuracy for using lab-data to classify field images is given, to enhance the potential of former lab-studies for future field detection and monitoring of macroplastics.

With this paper, we aim to bridge the gap between experiments in controlled and natural environments. The usage of existing lab- data and methods for natural environments could accelerate the harmonization of plastic monitoring in polluted aquatic environments.

2 Methods

2.1 Riverbank-harvested plastic samples

In this study, riverbank macrolitter was harvested from two different locations for the hyperspectral imaging in both environments. For the controlled environment, the items were harvested from the north Riverbank of the Rhine River near Rhenen (51°57'12.6"N 5°34'31.5"E), in a 100 meter (parallel to river) by 25 meter sampling area. These items were collected as part of the riverbank litter monitoring programme "Clean Rivers" [24]. After categorisation based on the River-OSPAR protocol as applied in van Lieshout et al. [25], all litter items were scanned floating in water using a VIS-SWIR (400-1700 nm) double-camera setup as described in Tasseron et al. [5]. For this study, only the NIR-SWIR range (1150 – 1675 nm) was used for all analyses. In total, 78 items were scanned, consisting of 58 plastic items and 13 aluminium items (Fig. 1a-d). The remaining eight items are a miscellaneous collection of paper, rubber and glass which were not used in subsequent analyses.

Figure 1: Riverbank-harvested items from Rhenen used for hyperspectal imaging in controlled environment (a-d); frame with riverbank-harvested items from Maastricht used for hyperspectral imaging in natural environment (e).

For the hyperspectral imaging in a natural aquatic environment, plastic litter items harvested in a 100 meter by 5 meter area from the Meuse riverbank near Griendpark, Maastricht (50°51'15.5"N 5°41'50.0"E) were used. These items were collected as part of a floating macroplastic monitoring programme "Pilot monitoring floating litter and macroplastics in the Dutch Rhine and Meuse rivers" [26]. In total, 26 plastic items were arranged in a wooden frame (Fig. 1e). This collection consists of a variety of hard plastics (high-density polyethylene (HDPE), polypropylene (PP)), soft plastics (low-density polyethylene (LDPE)), foams (polystyrene (PS), expanded polystyrene (E-PS)) and polyethylene terephthalate (PET) bottles. The diverse colours of the items helps to understand how darker coloured items are reflecting light differently from lighter coloured items.

2.2 Experimental setups - controlled environment and natural environment

The hyperspectral imaging in this study was all conducted in the near-infrared (NIR) to shortwave infrared (SWIR) part of the electromagnetic spectrum, spanning from 1150 to 1675 nm. Different cameras were used for both environments, as described in the next sections.

2.2.1 Controlled lab environment

The hyperspectral imaging of the riverbank-harvested litter in the controlled environment was performed using the Specim FX17 camera (Konica Minolta Company, Oulu, Finland). This line-scanning camera covers the electromagnetic spectrum between 900-1700 nm in 112 spectral bands. All technical information regarding the integration time, resolution and effective pixel size of this camera as well as the illumination and relative reflectance conversion is summarised in Tasseron et al. [5]. Fig. 2a shows the experimental setup used in Tasseron et al. [5]. The imaging of the riverbank litter was performed prior to this study. The raw image data was unexplored by Tasseron et al. [5] and was downloaded online for further analysis in this study [27]. Only the data from the Specim FX17 camera was used, since the spectral range of the Specim FX10 camera as shown in Fig. 2a is outside the scope of this study.

2.2.2 Natural aquatic environment

Hyperspectral images were taken in a natural environment using the sample items depicted in Fig. 1e and the setup shown in Fig. 2b. We used the Snapscan SWIR hyperspectral imaging camera (IMEC, Leuven, Belgium) which covers the electromagnetic spectrum from 1150 to 1675 nm in 100 equally spaced spectral bands. It captures with an integration time ranging from 20ms – 65ms, depending on acquisition parameters, lighting, and the reflectance characteristics of the objects. The camera has a maximum spatial resolution of 1200 x 640 pixels, although a smaller resolution of 520 x 640 pixels was used for this study.

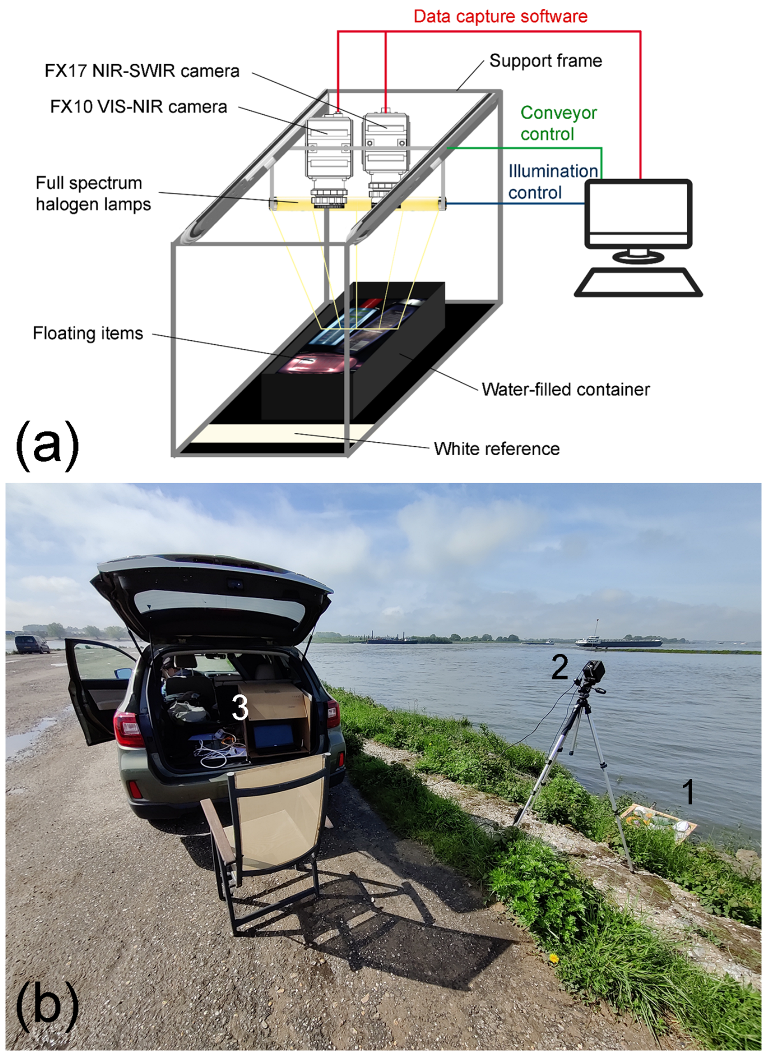

Figure 2: Hyperspectral imaging setup used by Tasseron et al. [5] (a); Hyperspectral imaging setup in the natural environment (b) with riverbank-harvested sample items (1), IMEC Snapscan SWIR hyperspectral camera (2), laptop with data capture software and power source (3).

As opposed to the Specim FX17, the Snapscan SWIR camera has an integrated line scan sensor which allows using a tripod for scanning the samples.

The hyperspectral images were taken on a groyne of the Waal River, near Ochten, the Netherlands (N 51°54'13.3" E 5°33'52.7"). This location was chosen because it is characterised by diverse background elements such as sand, rocks, gravel, and various types of vegetation which are the main components composing Dutch riverbanks [28]. Moreover, the ability to park a car in close vicinity of the river allowed powering the camera with the car's battery without the need of expensive deep-cycle batteries.

On the 28th of May 2021, hyperspectral data was acquired in a cloud-free setting between 11:07 and 12:19. During the experiment, the solar altitude angle ranged from 48.35° – 56.26°, and the azimuth from 122.61° – 146.95°, illuminating the samples from the south-east. In order to account for these changing conditions, the camera's white reference was recalibrated every five minutes by using a white sheet of optical grade Spectralon, similar to the white reference used in Tasseron et al. [5]. Images were shot with various integration times, to ensure optimal exposure of both light and dark-coloured sample items.

2.3 Data preparation and ROI selection

To allow the comparison of the spectral signatures between the two environments, several data pre-processing steps had to be undertaken. First, the hyperspectral data of the controlled environment underwent manual reflectance correction (1) and intensity normalisation (2) prior any subsequent analysis [5]. An overview of the constituents of these equations is found in Appendix A (Table 1). For the hyperspectral imagery in the natural environment, the reflectance correction and intensity normalisation were executed directly by the data capturing software using the same equations. The reflectance correction was done using averaged reflectance values per wavelength

$$R_n = (R_0 - R_B)/(R_W - R_B) \tag{1}$$

$$R_{ni} = (R_n - min(R_n))/(max(R_n) - min(R_n)) \tag{2}$$

Next, regions of interest (ROIs) were manually annotated on the imagery data of both environments, using the PerClass Mira toolbox in MATLAB. Similar to Tasseron et al. [5], a paintbrush tool was used to define each ROI according to a distinct class. For the lab environment, three classes were established, with a group of pixels being either: (1) water, (2) vegetation or (3) plastic. A total of 786,264 pixels were annotated. For the data captured at the Waal River, the ROIs were assigned one of the following six classes: (1) water, (2) vegetation, (3) wood, (4) rock, (5) plastic, and (6) sand. For each of these classes in both environments, the average spectral signatures were calculated. An overview of the ROI selection of the data captured in the natural environment is shown in Fig. 3.

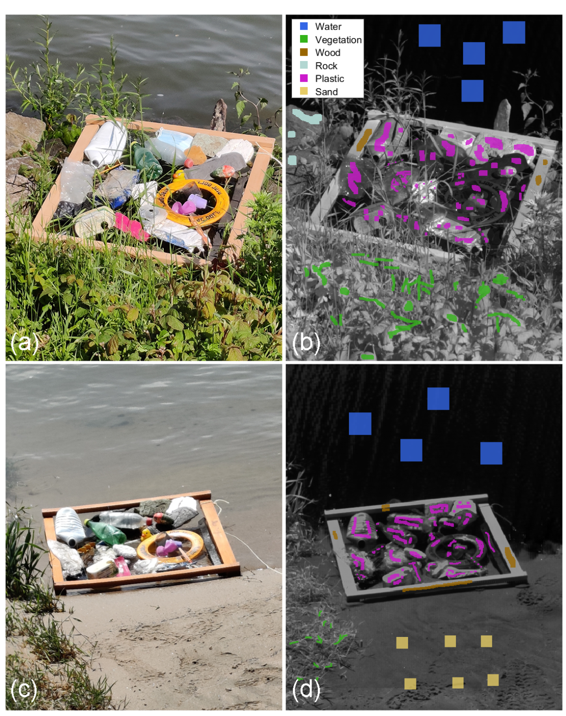

Figure 3: Annotated ROIs on the two images constituting the natural environment pixel dataset used for further analysis (b,d) and their respective RGB-images (a,c). The ROIs in b and d consist of 23.804 and 16.485 pixels, respectively.

Since the spectral range and resolution varied for both cameras, three manipulations were done on the data acquired in the lab. First, the range of the average spectral signatures was matched by discarding the data outside the 1150 − 1675 nm range. Second, the remaining 74 hyperspectral bands were linearly interpolated to match the 100 bands of the Snapscan SWIR camera. Third, a manual selection of the Snapscan SWIR bands that were closest to the Specim FX17 bands resulted in an imagery dataset of both cameras with 74 hyperspectral bands. More advanced and scientifically robust techniques for matching hyperspectral ranges exist (e.g., [29, 30]]) but are outside the scope of this study. All three manipulations are done in MATLAB.

2.4 Support Vector Machine (SVM) and Spectral Angle mapper (SAM) classifiers

Two types of classifiers are applied on the dataset to understand their applicability in linking laboratory experiments and field observations. First, a support vector machine algorithm is used with training data from both lab- and field observations using the perClass toolbox in MATLAB. The main advantages of support vector machines is their robustness to noisy and complex input data [31], the small number of training samples needed [32] and the ability to efficiently handle high dimensional hyperspectral datasets [33]. Main drawbacks of SVMs include the time-consuming process of selecting a suitable kernel function and model training, especially with larger datasets [34], the lack of a probabilistic explanation for the classification, and a higher risk of overfitting [35]. Overfitting occurs when an algorithm or model works well on a training dataset, but performs poorly on testing datasets [36].

Next, the Spectral Angle Mapper (SAM) algorithm, Spectral Information Divergence (SID) and a logarithmic combination of the two (SID-SAM) algorithms from the hyperspectral Image Processing Toolbox™ are tested. A detailed explanation of how these algorithms work is found in appendix C. These algorithms have several advantages in comparison with SVM-based classifiers. For instance, they are almost insensitive to differences in the intensity values of a signal [37]. In addition, SAM classifiers are easy and accurate methods for mapping the spectral similarity of a given pixel to a reference spectrum or a set of reference spectra [38]. One main disadvantage of SAM classifiers is that ever pixel is labelled based on the closest reference spectrum, implying a pixel that does not belong to any of the predefined categories is classified incorrectly. This can easily be resolved by setting boundaries beyond which pixels should not be classified. To demonstrate the influence of narrowing the decision boundaries, the SAM-classifier is computed using three decision boundary angles of 7.5°, 10° and 15°. Another disadvantage is that these classifiers to not consider mixed pixels and sub-pixel values [38], yet this is not an issue with the resolution and quality of the hyperspectral data used in this study but can be problematic using satellite or UAV images.

3 Results and discussion

First, it is established which reflectance patterns characterise riverbank-harvested litter in a controlled environment. A similar procedure is followed for macroplastics in aquatic ecosystems and a comparison between the two environments is made. Second, the accuracy of the SVM, SAM, SID, and SID-SAM classifier algorithms in the identification of plastics in both environments is established. The SID and SID-SAM algorithms showed significantly lower classification accuracies than the SAM algorithm.

3.1 Reflectance patterns of water, vegetation, and plastics in various environments

Fig. 4 shows the average reflectance signatures of water, vegetation and plastic in lab and field-based experiments from 1150 – 1675 nm. Clearly, multiple differences are present between the lab and field-based signatures in all three classes.

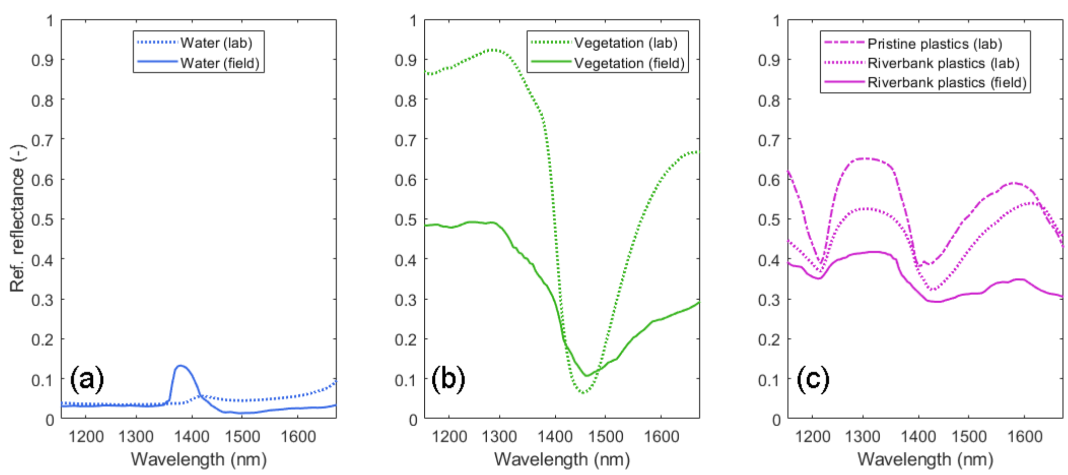

Figure 4: Lab and field-based reflectance signatures of: (a) water, (b) vegetation, and (c) plastic. Dotted lines indicate signatures as measured in the controlled environment. The 'dash-dot' line in (c) is the average spectral signature of pristine plastics as determined by Tasseron et al. [5], which is used just for a frame of reference.

First, the spectral signature of water has similar intensities over the entire hyperspectral range, with one exception. A slight reflectance peak is apparent in the water reflectance measured in the field between approximately 1370 and 1430 nm. This artificial peak was caused by a relative low signal-to-noise ratio of the hyperspectral imaging sensor outdoors. When comparing the range of this peak with the spectral energy curve of solar radiation, a strong absorption window of H_2O molecules is present [39]. In fact, the transmittance of the atmosphere is almost zero at the wavelength where the water reflectance in Fig. 4a peaks [40]. Even though the use of a white reference cancels out differences in atmospheric transmittance, the large amount of noise caused by the extremely low transmittance is most likely the cause of this apparent peak in the spectral signature.

Comparing the two spectral signatures of vegetation, an important dissimilarity between the signatures is a large difference in the intensity. A likely reason for this dissimilarity is the difference in integration time of the sensors and illumination intensity of the samples in both environments. Additionally, the leaf water content significantly influences the strength of the absorption peak at 1450 nm [41], which could be different for both environments. The overall shape of both signature is relatively similar, having a high reflection between 1150 – 1300 nm, an absorption peak around 1450 nm and a steady increase in reflection between 1450 – 1675 nm. As mentioned earlier, SVM-based classifiers are more sensitive to differences in intensity than SAM classifiers. The latter could result in a more robust and accurate classification for SAM classifiers in comparison with SVM-based classifiers. Third, the spectral signatures of plastics are shown in Fig. 4c. Like vegetation, the overall shape with absorption and reflection peaks is comparable between the three different signatures. Key differences between the lab-based and field-based spectral signatures of riverbank-harvested plastics is the intensity and strength of the absorption peaks. With controlled and stable light conditions, the average lab-based signature is relatively smooth with a range of approximately 0.37 – 0.52 in intensity. In contrast, the average field-based signature is less smooth and has a smaller intensity range, in which the absorption peaks are slightly less pronounced. Tasseron et al. [5] emphasised the importance of the absorption peaks in distinguishing plastics from vegetation and water. Luckily, the atmospheric absorption of H_2O molecules is not in overlapping with the wavelengths of the absorption peaks of plastics, which subdues the influence of sunlight in the classification of plastics.

3.2 Classifier algorithms for identification of plastics in both environments

3.2.1 Support Vector Machine pipelines

A distinctive property of the SVM pipelines is to separate between the six different classes of the ROIs used for training, which each have a unique spectral signature. Fig. 5 shows two classified images using the 'pipeline_svm' (trained using ROIs from Fig. 2b) and 'pipeline_svm_field' (trained using ROIs from Fig. 2d) pipelines. It is evident that the RBF kernel used in these pipelines performs well when using ROIs from the same image yet is not very robust when using a training dataset based on a different image. This emphasizes the high risk of overfitting with SVM classifiers. In fact, the confusion matrix in Fig. 9a (Appendix B) shows that the user's accuracy of the plastic class is only 30.1%. Most pixels that should have been classified as plastic, are classified as sand and vegetation instead. In addition, a large share of the pixels that should have been classified as water are classified as plastics. This is not reflected that in the confusion matrix in Fig. 9b (Appendix B), as it states 93.8% of water pixels are classified correctly. The latter is caused by the chosen ROIs for computation of the confusion matrix. As seen in Fig. 3b, the annotated ROIs for water mostly cover the pixels that were classified correctly.

When using the pipelines including lab data for training, the classification is significantly different. Fig. 6 shows the classified images using a combination of lab and field data, and only field data. Clearly, the classification of plastic pixels using lab data in combination

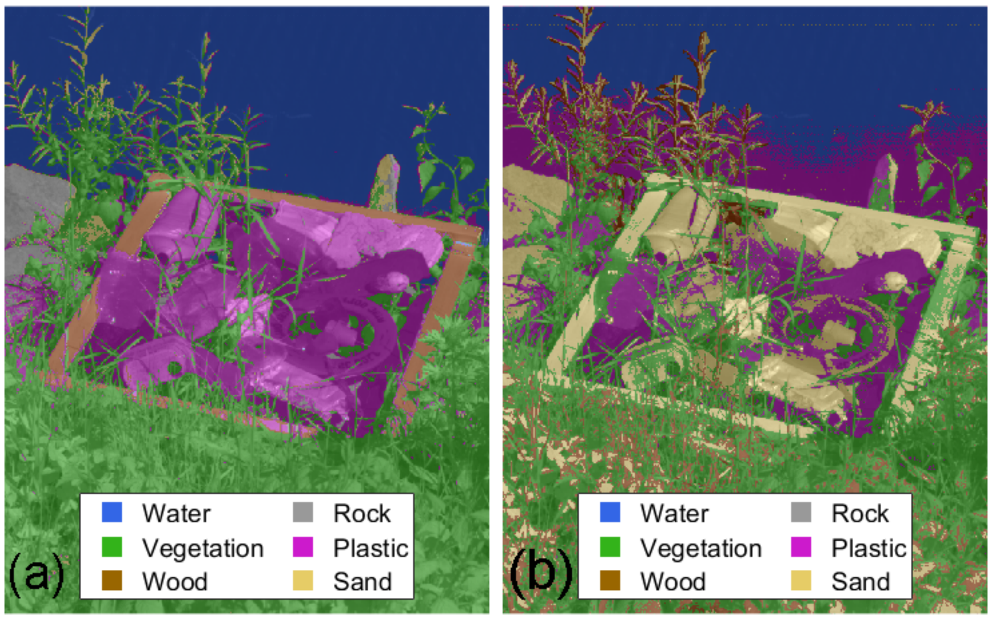

Figure 5: Support Vector Machine classified images using: (a) ROIs of the same image to classify the entire image, and (b) ROIs of Fig. 2d - different image - used for training the classifier. Associated confusion matrices are found in Fig. 10 (Appendix B).

with field data for background elements yields poor results. As depicted in Fig. 6a, nearly all plastic pixels are not classified at all or classified incorrectly, with a user's accuracy of 4.3% (Appendix B, Fig. 10). This extremely low accuracy is likely caused by the difference in signatures derived from lab-data and field-data.

Classification accuracies of plastics significantly improve when using only laboratory-based data, as depicted in Fig. 6b, 6c. The difference between these two classifications clearly demonstrate a weakness of SVM-classifiers, specifically its sensitivity to changes in intensity. The intensity of the average lab-based vegetation spectrum is much higher than the spectrum based on field data. Therefore, the SVM-classifier decided the vegetation pixels in Fig. 6b better resemble the plastic spectrum based on intensity, which resulted in a complete misclassification of vegetation. Halving the intensity values of the vegetation pixels used for training results in a slightly better classification (Fig. 6c). Yet, the producer's accuracy of plastic pixels is still only 68.2% (Appendix B – Fig. 10), which substantiates the dependence on intensity in SVM-based classifiers.

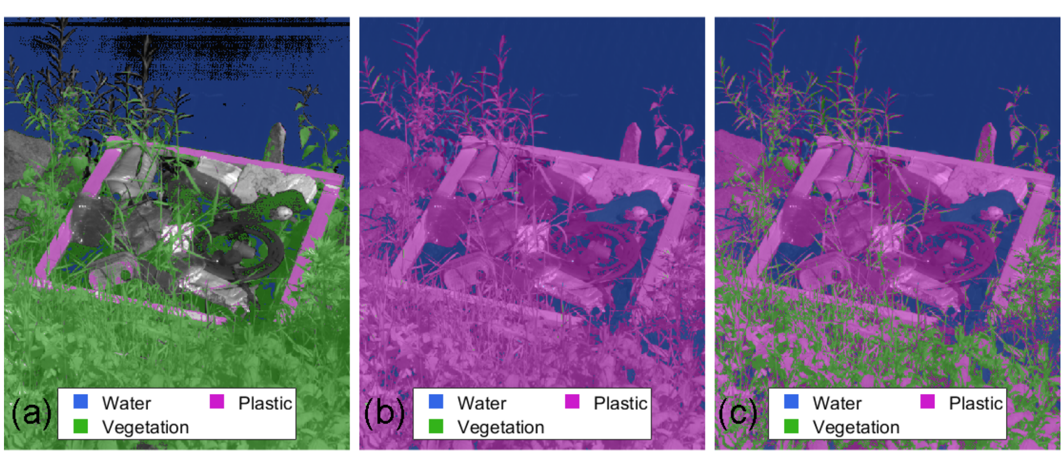

Figure 6: Classified images using support vector machine pipelines with (a) lab data for plastics, field data for vegetation and water, (b) lab data for all categories, and (c) lab data for all categories, with halved intensity of the vegetation pixels.

3.2.2 SAM, SID and SIDSAM

This section illustrates and quantifies the differences between SAM, SID and SIDSAM classifications. First, by using field-data to train the algorithms, followed by using lab-data for training. Lastly, the effect of narrowing the cone of uncertainty of SAM-based classifications is illustrated. Fig. 7a-c depict the classification results of using these three algorithms trained with field-data. It is clear the SAM algorithm performs best, with a user's accuracy of 93.5% for plastics (Appendix B – Fig. 11), as opposed to 18.2% and 68.6% for SID and SIDSAM, respectively. However, the rock in the image is classified as plastic when using SAM, whereas it is classified as sand using the other two algorithms (Fig. 7a-c). Even though the rock is classified incorrectly, the producer's accuracy is higher for SID and SIDSAM (99.5% and 99.2%, respectively) than for SAM (85.8%).

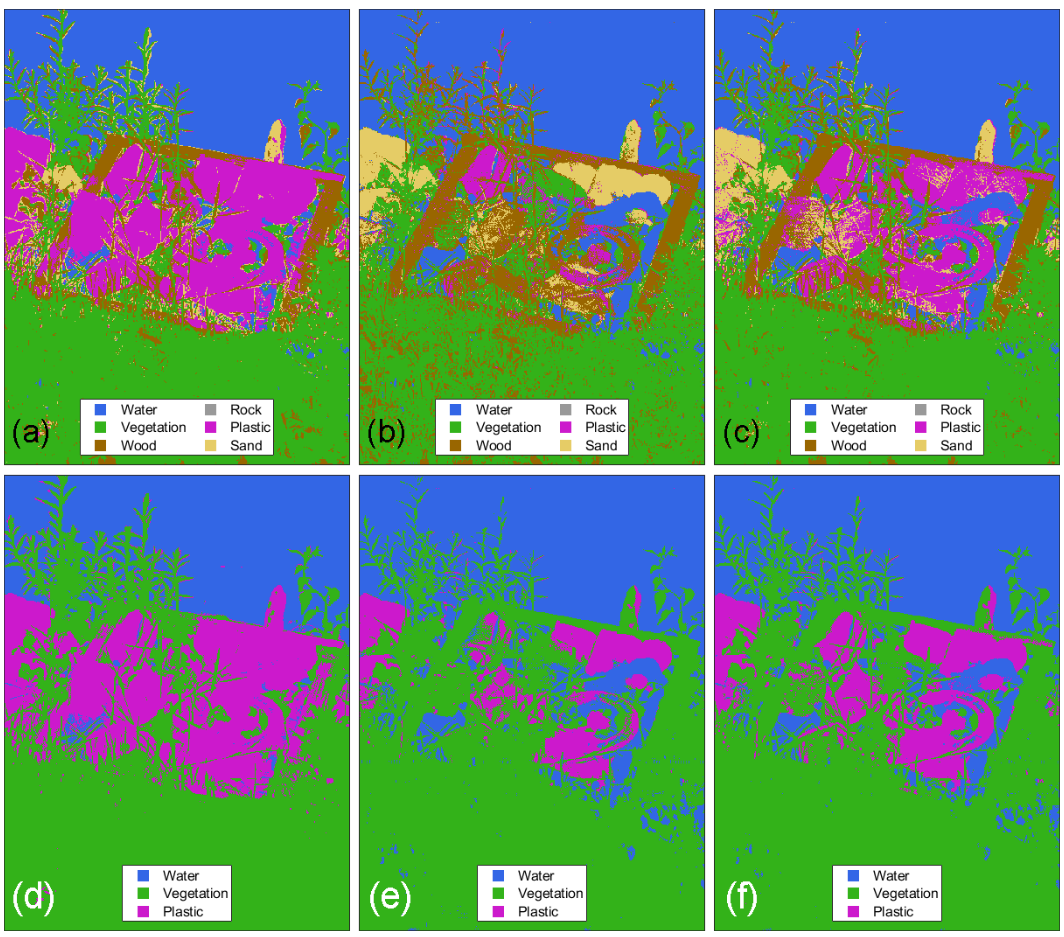

Figure 7: Classifications with training dataset based on ROIs of Fig. 3d, using (a) SAM, (b) SID, (c) SIDSAM, and and Classifications with training dataset based on lab-data, using (d) SAM, (e) SID, (f) SIDSAM

The SID algorithm, using a probabilistic approach based on intensity, misclassifies most plastic items with a low intensity. For example, the plastic bottle in the top left of the Frame (Fig. 7b) seems to be the only item recognised as plastic by this algorithm. Referring to Fig. 1e, this bottle (id 1) is opaque and white, which means it has a significantly higher reflection value than all the other plastic items. Therefore, it is likely the low user's accuracy for plastics of this algorithm is caused by higher intensities in the training dataset. In fact, the black foam (Fig. 1e – id 9) is classified as water both for SID and SAM. This misclassification makes sense when considering the probabilistic nature of intensities. Since darker coloured items have lower reflectance intensities, the darker plastic items are more likely to resemble the spectra of wood, sand, vegetation or even water. From Fig. 7c, it is clear this effect is smaller when using SIDSAM, but still yields a smaller user's accuracy for plastic items.

Next, when using only lab data for classification, similar patterns between the three algorithms are found, as depicted in Fig. 7d-f. A user's accuracy for plastics of 93.6%, 50.2% and 65.4% is reached for SAM, SID and SIDSAM, respectively (Appendix B – Fig. 12). The producer's accuracy for plastics is 99.8% for SAM, and 100% for SID and SIDSAM, indicating that nearly no vegetation or water pixels were classified as plastic. It is evident the SID and SIDSAM algorithms perform worse when classifying pixels with a low reflectance intensity. In fact, darker coloured items are misclassified in a similar fashion when compared with the algorithms trained with field-data.

3.2.3 SAM with various decision boundaries

This section illustrates the influence of different decision boundaries at 7.5°, 10° and 15° using SAM, Fig. 8a-c shows the classification results using field data as a training dataset. As illustrated in Fig. 13 (Appendix B), an advantage of narrowing the cone is that both the user's and producer's accuracy of plastics increase. For example, most pixels that compose the rock in Fig. 8a are classified as plastic. With a narrower decision boundary cone, the same rock region in Fig. 8c mainly consists of unclassified pixels.

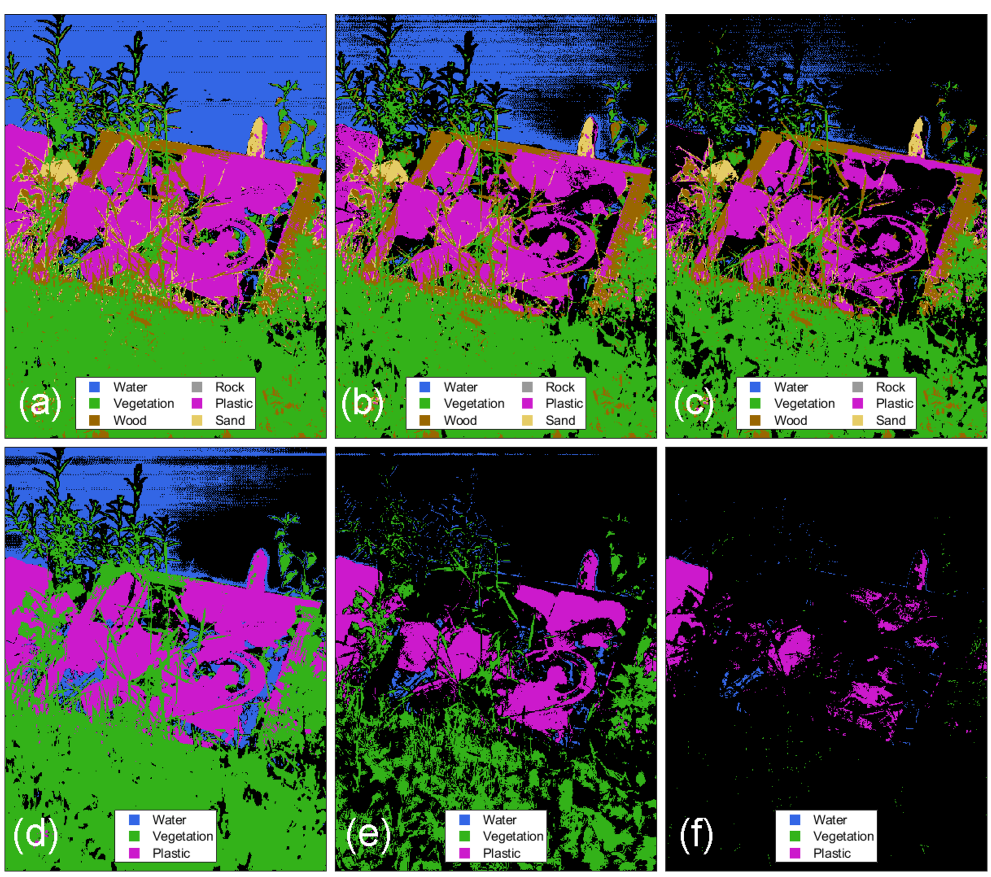

Figure 8: SAM classification using field data with decision boundaries set at (a) 7.5°, (b) 10° and (c) 15°, and classification using lab data with decision boundaries set at (d) 7.5°, (e) 10° and (f) 15°. Black pixels indicate unclassified pixels, that do not fall within the decision boundary region.

When applying the same decision boundaries on the classifier using lab data as reference spectra, a few major differences are present (Fig. 8d-f). For example, almost all vegetation and water pixels become unclassified when using a decision boundary of 7.5°. For plastics, a cone of 15° leads to approximately 8.0% of plastics being missed, whereas the cone of 7.5° results in 85.6% of plastic pixels being missed. As elaborated in section 4.1, several differences in the reflection spectra of lab- and field-based imaging are present. It is likely these differences are large enough to cause most pixels in all categories being unclassified when using the 7.5° decision boundary. As illustrated in Fig. 14 (Appendix B), the increase in user's and producer's accuracy is only marginal, which is rendered futile when considering the large share of missed pixels with narrowed decision boundaries. Lastly, the rock is still classified as plastic, whereas most pixels that should be classified as plastic are being missed (85.6%). Therefore, the effect of narrowing the decision boundary when using lab-data to classify field-data is mainly disadvantageous.

However, it is also evident that narrowing the decision boundary results in an increased number of unclassified pixels. In fact, Fig. 15 (Appendix B) shows the percentage of unclassified pixels with a narrowing decision boundary region. For the classification with field data, a cone of 15° results in a loss of approximately 3.7% of the pixels that should be classified as plastic. This quickly increases to 42.1% when a cone of 7.5° is used. Therefore, it is necessary to find a balance between the number of missed pixels and the accuracy of the classification.

4 Synthesis and Outlook

Based on the knowledge that macroplastics reflect light in a unique way compared to other floating litter and natural or anthropogenic background materials [5–19], this study addressed two objectives. First, an understanding of the difference between lab-based and field-based hyperspectral imaging was made by comparing the associated hyperspectral signatures. The riverbank-harvested plastic samples investigated for this purpose were presumed to be an appropriate subset of commonly found litter along Dutch riverbanks, corroborated by van Emmerik et al. [42]. Second, it was investigated how plastics can best be distinguished from background elements and materials by exploiting various classification approaches. In doing so, a foundation for using laboratory data to train models that classify field-images was successfully made.

The results strongly suggest lab-based data can be used in a spectral angle mapper (SAM) algorithm to classify hyperspectral images taken in the field. Previous studies indicated SAM is relatively robust to changes in illumination intensity and mapping spectral similarities compared to other classification methods [37,38,43]. Therefore, the detection of plastic items was still successful even though the environmental factors are highly different from lab conditions. The large number of annotated pixels from the lab-based images (n = 786,264) allowed the establishment of representative hyperspectral signatures of plastics.

Additionally, a high-resolution field image (n = 332,800 pixels) allowed thorough analyses of different classification techniques. As a result, the fundamental method resulted in accuracies of up to 93.6% for plastics when classifying an image captured at the riverbank. In doing so, our results are amongst the first to tackle the challenge of using lab-based data for field-classification of plastics, which was emphasised by Martínez-Vicente et al. [22].

Yet, one of the main challenges for future hyperspectral field detection of plastics includes the dynamic nature of meteorological conditions [44, 45], which can significantly affect the image capturing process. In fact, the long integration time of up to 10 seconds per capture required the samples to be completely stationary. Additionally, rapidly changing light conditions such as shadows casted on the objects by clouds required continuous sensor recalibration. Thirdly, extremely low atmospheric transmittance between 1350 – 1400 nm causes excessive noise in this region of the spectrum, which can be amplified in normalisation techniques. Therefore, it is recommended for future studies to omit such wavelength ranges in their analyses. These factors combined are a major complication for fundamental detection and eventually long-term monitoring. In fact, Stuart et al. [44] argue that even state-of-the-art hyperspectral systems are challenging to use in continuous field monitoring, especially in volatile environments which require outer casing of devices to be weatherproofed [46]. Moreover, long term detection and monitoring of floating litter is technologically restricted by the spatial, spectral, and radiometric resolution of existing hyperspectral sensors [20]. Yet, the continuous development of (ultra) compact, lightweight and affordable multispectral and hyperspectral imaging systems (e.g. [47]) is promising for future monitoring missions.

A key step for further practical application of hyperspectral imaging includes the establishment of reliable and high-quality reference libraries. Various open-access libraries with reference hyperspectral signatures already exist. For instance, the ECOSTRESS spectral library consists of over 3000 hyperspectral signatures of manmade materials, soil, water and vegetation [48]. Developed by NASA, this library is widely used in estimating vegetation abundance and classifying mineral surfaces [49, 50]. Including hyperspectral signatures of plastics as found in [5–19] and this study in such reference libraries is essential. This can either be done as an addition to existing libraries, or by the establishment of a completely new open-access library specifically designed for plastics. All hyperspectral data used for the analyses in this study are available online in such a reference library (data availability statement). The signatures included in these libraries would have a high spectral resolution. This implies a smaller range of bands or even multispectral bands can be selected or interpolated, which can in turn be used in comparison with new field measurements. In addition, the continuous development of (ultra) compact, lightweight and affordable hyperspectral imaging systems (e.g. [47]) is promising for future plastic detection and monitoring missions.

5 Conclusion

Hyperspectral imaging systems provide new opportunities for the detection and the identification of macroplastics in natural environments. First, this study explored the differences and similarities between lab-based and field-based hyperspectral signatures of water, plastic, and vegetation. These findings were in turn used to understand the differences in performance of various classifier algorithms, and which algorithm performs best. A key factor influencing performance of SVM, SID, and SIDSAM classifiers is the reflectance intensity of the hyperspectral signals. On the contrary, SAM is relatively robust concerning the reflectance intensity and performs best out of these four techniques. Future work should explore the influence of the illumination differences in more detail, as well as the role of additional changing environmental conditions and its impacts on hyperspectral monitoring.

Second, this study successfully demonstrated the use of laboratory-based hyperspectral measurements for identification of plastics in a natural aquatic environment. The latter was realised by using various classification algorithms and assess their effectiveness in detecting plastics using confusion matrices. With accuracies of up to 93.6%, the spectral angle mapper (SAM) algorithm was most successful in separating plastic items from natural background elements. Future work exploring the fundamental applications of similar algorithms should include a wider range of imagery captured under various environmental conditions. This is in turn relevant for long-term detection and monitoring of plastics using hyperspectral systems.

Continuous technological advances in combination with the fundamental findings in this study and similar studies will eventually lead to monitoring of plastic debris in aquatic ecosystems that is more reliable and consistent than visual or manual counting. Yet, there are still some major developments required before this is realised. As soon as harmonised methods to automatically monitor the presence and abundance of plastics exist, targeted action can be taken at the source of the pollution, rather than at the aquatic ecosystems in which the litter would otherwise end up.

Conflict of interest

The authors declare that the research was conducted in the absence of any commercial or financial relationships that could be construed as a potential conflict of interest.

Author contributions

Conceptualization: PT, Methodology: PT Formal Analysis: PT Investigation: PT, LS JAP Visualization: PT Data curation: PT Writing–original draft: PT Writing–reviewing and editing: all authors Supervision: JAP, LS, TvE Project administration: PT Funding acquisition: TvE

Data availability statement

All MATLAB scripts and associated data are available online at https://github.com/PaoloTasseron/Hyperspectral_dataset

Acknowledgments

The authors would like to thank Lei Zhang (IMEC/One Planet), who enabled the trips to the field with the hyperspectral camera. Aditionally, the authors would like to thank Marco Balsi ("La Sapienza" University of Rome, Italy) for his efforts in providing his expert opinion and reviewing the draft manuscript prior to submission, improving the quality of the work.

Appendix A - Tables

Table 1: Constituents of the equations and their description.

Constituent	**Description**
R_n	Corrected relative reflectance imagery (FX17)
R_0	Raw reflectance dataset (FX17)
R_B	Mean dark reference reflectance (FX17)
R_W	Mean white reference reflectance (FX17)
R_{ni}	Normalised intensity dataset (FX17)

Table 2: Constituents of the equations and their description.

SVM Pipeline name	**Training data**
pipeline_SVM	ROIs Fig. 3b
”_field	ROIs of Fig. 3d (different training – validation dataset)
”_lab	ROIs Fig. 3b (excluding plastics), and Plastics from lab data (R_{ni})
”_onlylab_10k	Random selection of 10.000 pixels from lab data (R_{ni}) vegetation, riverbank-harvested plastics and water
”_onlylab_10k_vegetation_halved	Random selection of 10.000 pixels from lab data (R_{ni}) vegetation, riverbank-harvested plastics and water. Intensity of vegetation multiplied by 0.5.

Appendix B - Figures

The confusion matrices are characterised by two columns of percentages, labelled 'True Class' (user's accuracy) and 'Predicted Class' (producer's accuracy). The blue tinted values indicate the % correctly classified pixels ('accuracy'), whereas the red tinted values indicate the % incorrectly classified pixels.

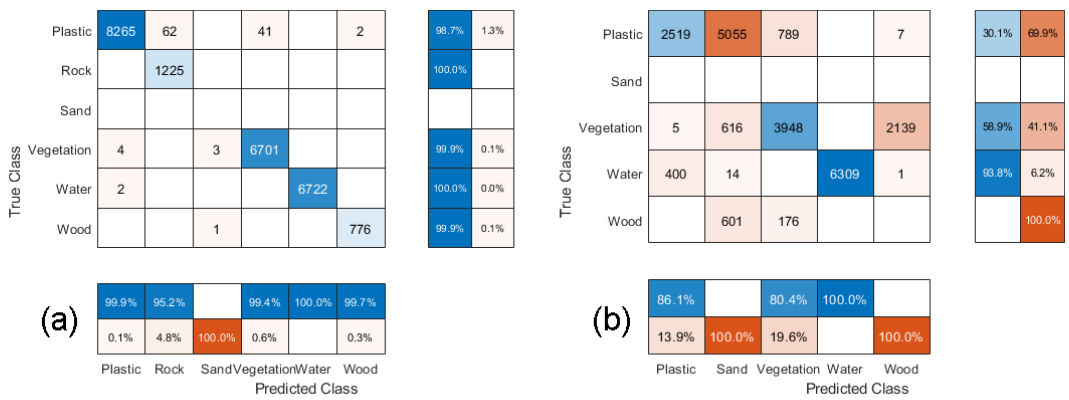

Figure 9: Confusion matrices for SVM-classified image based on (a) ROIs from the same image to classify the entire image, and (b) ROIs of Fig. 2d (Different image) to train the classifier.

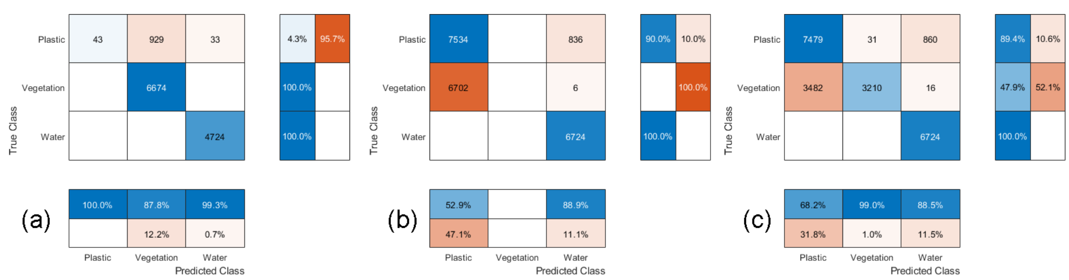

Figure 10: Confusion matrices for SVM-classified image based on (a) lab data for plastics, field data for vegetation and water, (b) lab data for all categories, and (c) lab data for all categories, with the intensity of the vegetation pixels multiplied by 0.5

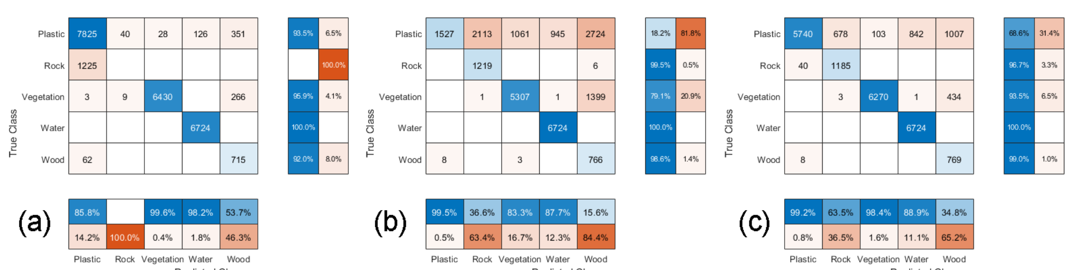

Figure 11: Confusion matrices for: (a) SAM, (b) SID, (c) SIDSAM using field data (ROIs Fig. 3b) for training

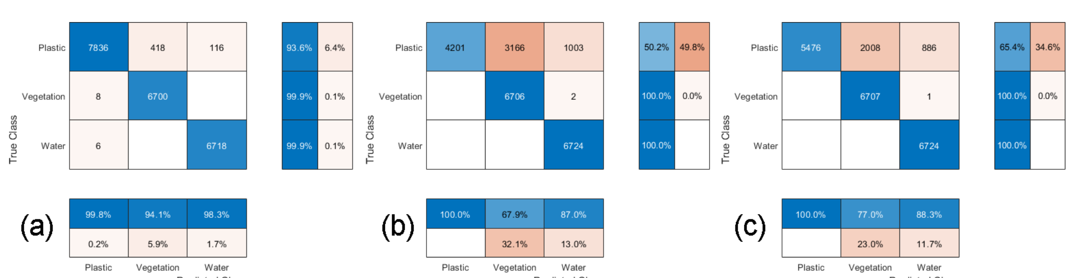

Figure 12: Confusion matrices for: (a) SAM, (b) SID, (c) SIDSAM using lab data for training.

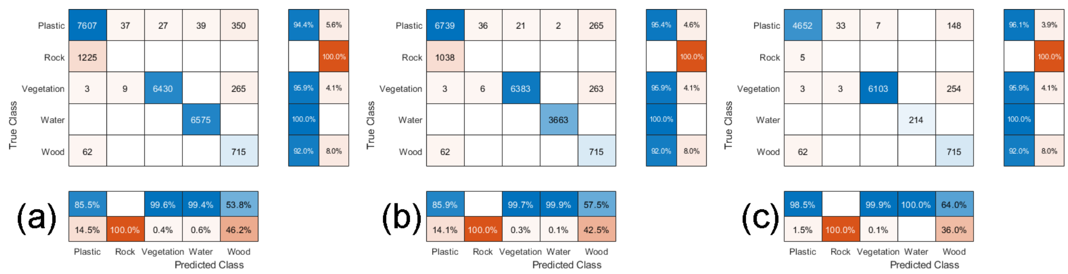

Figure 13: Confusion matrices for SAM-classified image based on field data, with: (a) 15° cone, (b) 10° cone, and (c) 7.5° cone.

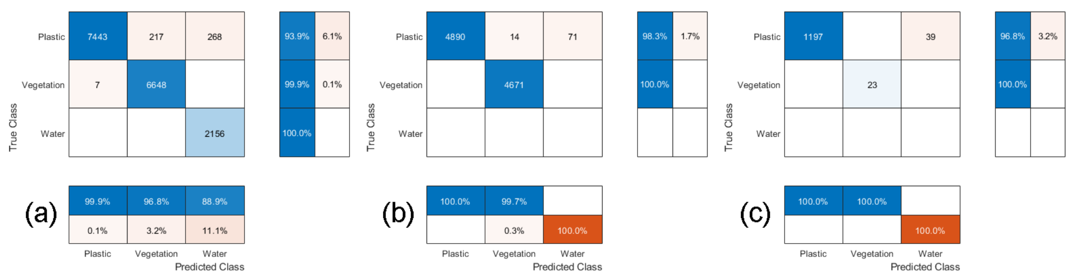

Figure 14: Confusion matrices for SAM-classified image based on lab data, with: (a) 15° cone, (b) 10° cone, and (c) 7.5° cone.

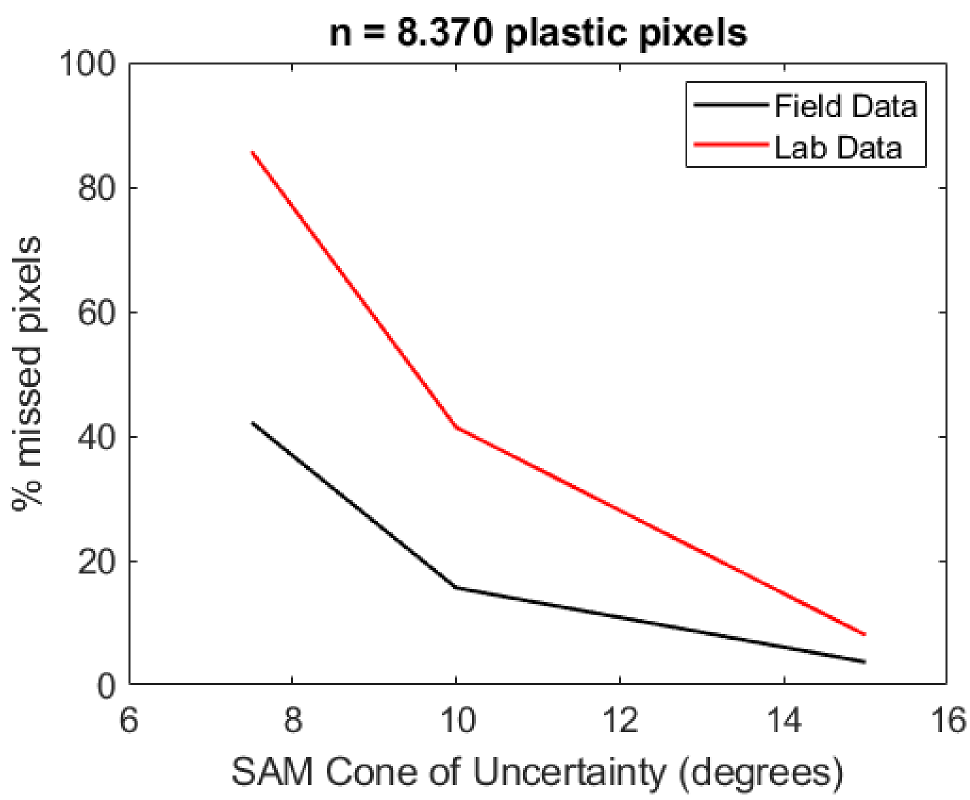

Figure 15: Percentage of missed pixels in classification plotted against the cone of uncertainty (decision boundaries) for field data and lab data.

Appendix C - Algorithm explanation

5.1 Support Vector Machine in MATLAB

The support vector machine (SVM) algorithm is used in MATLAB based on libSVM [51]. As mentioned earlier, selecting a suitable kernel function for model training is time-consuming, so a default Radial basis function (RBF) kernel is used. An explanation of the mathematics behind this kernel is outside the scope of this study. However, it is important to note the function has two customisable parameters: σ and C. The sigma parameter determines the reach, which defines the importance of points close to the decision boundaries of the classes. A high σ value indicates the decision boundaries are highly flexed, whereas a low value indicates a more linear decision boundary. Next, the C parameter determines how much misclassification is allowed. Smaller values of C indicate a large margin of error, allowing a substantial number of misclassifications, whereas a high value of C indicates a small margin of error. Like the default RBF function, the default σ and C values are used in classification. Since the SVM algorithm is used for solving a multi-class classification, the default one-against-all strategy is used. This method constructs n_i (number of classes) classifiers in which each classifier separates class i from all other classes [52]. These classifiers are then combined for a decision which class the pixel spectrum fits best.

Several training datasets are used to train five different classification pipelines. An overview of these pipelines is summarised in Appendix A (Table 2). As a baseline reference, the first pipeline is trained using the ROIs as indicated in Fig. 3b to classify the same image used for training. Next, the second pipeline is trained using the ROIs from Fig. 3d, to classify the hyperspectral data belonging to the image in Fig. 3a. This pipeline was trained to assess the influence of using input data from a different field image in SVMs. Thirdly, a pipeline is trained using all ROIs from Fig. 3b, except for plastics. The spectral signatures of riverbank-harvested plastics obtained in the lab are used in this pipeline. This pipeline was trained to assess to what extent a combination of using lab and field-based input data is possible. The fourth pipeline is trained using only lab data, with three classes: plastic, vegetation, and water. This pipeline is in line with the main aim of this study, to assess how lab-data can be used for field classification. Lastly, the fifth pipeline is trained using the same data as the fourth pipeline, with the intensity of the vegetation pixels multiplied by 0.5. This is done to emphasise the case that support vector machines are sensitive for changes in intensity values. Confusion matrices are computed for all pipelines to understand the effect of using different combinations of training datasets on the accuracy of classification.

5.2 SAM, SID, and SID-SAM in MATLAB

Spectral angle mapper algorithms measure the spectral similarity between the spectra of each pixel in the input training dataset, and a specified collection of reference spectra [53]. It is based on the principle of computing the spectral angle distance between each pixel and the reference spectra in the dataset. The main output of the SAM algorithm is a vector or matrix with the spectral angle of each pixel relative to the reference spectra in radians. Low SAM scores indicate strong matches between the spectrum belonging to the tested pixel and the reference signature. A threshold angle can be set after which certain pixels should not be classified as the category belonging to the nearest reference spectrum (Fig. 16). Given the input data t with pixel index number i and reference spectra R_{ref} of length C, the SAM score α is calculated as:

$$\alpha = \cos^{-1} \frac{\sum_{i=1}^{C} t_i * R_{ref,i}}{\sum_{i=1}^{C} t_i^2 * \sum_{i=1}^{C} R_{ref,i}^2} \tag{3}$$

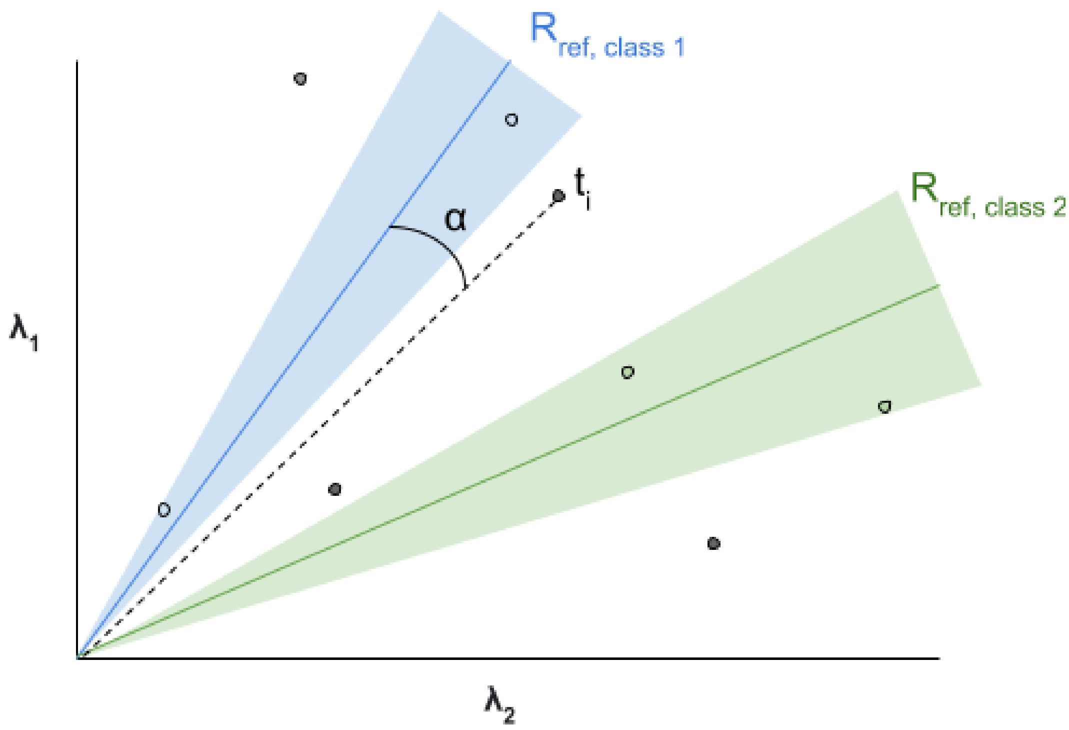

Figure 16: Visualisation of SAM, with two different reference spectra (green, blue) and their respective decision boundaries (shaded areas). The 'test' or 'input' pixel t_i value is given, with angle α relative to the reference spectrum.

Identical to SAM, the spectral information divergence (SID) algorithm measures the spectral similarity between the spectrum belonging to a pixel and a collection of reference spectra or endmember spectra. As opposed to SAM, this method calculates the spectral similarity based on the divergence between the probability distributions of the tested pixel and the reference spectra [54]. As such, the SID algorithm does not rely on geometric properties when measuring the discrepancy between the pixel spectra and reference spectra [55]. The main output of the SID algorithm is a vector or matrix with SID (divergence) scores. Smaller divergence values indicate a pixel spectrum is more likely to be similar to the reference spectrum [56]. Given the input data t with pixel index number i and reference spectra R_{ref}, the distribution values q_i for the input data are calculated as follows:

$$q_i = \frac{t_i}{\sum_{i=1}^{C} t_i} \tag{4}$$

The distribution values p_i for the reference spectra are calculated as follows:

$$p_i = \frac{R_{ref,i}}{\sum_{i=1}^{C} R_{ref,i}} \tag{5}$$

Using (4) and (5), the SID score β is computed as follows:

$$\beta = \sum_{i\ =\ 1}^{C} p_i * \ \log \frac{p_i}{q_i} \ + \ \sum_{i\ =\ 1}^{C} q_i * \ \log \frac{q_i}{p_i} \tag{6}$$

A combination of the SID and SAM algorithms improves the robustness of spectral matching, which can yield significantly better classification compared to using SID or SAM separately [57]. In their paper, Du et al. [57] showed that the combination of SID (β) and SAM (α) improved the detection and classification of sample panels with different spectral signatures. They proposed and tested the SIDSAM score γ, calculated (7). In addition to using SID and SAM separately, the SIDSAM score is also applied to see whether it provides a more accurate classification of the hyperspectral images used in this study.

$$\gamma = \beta * \tan(\alpha) \tag{7}$$

Lastly, the calculation of the SAM score allows the establishment of decision boundaries prior to classification. These are parameterised as the angle a given test pixel is allowed to diverge from the reference spectrum. Observations that do not fall within the decision boundaries of any reference spectrum are not classified.

References

[1] S. B. Borrelle, J. Ringma, K. L. Law, C. C. Monnahan, L. Lebreton, A. McGivern, E. Murphy, J. Jambeck, G. H. Leonard, and M. A. Hilleary, "Predicted growth in plastic waste exceeds efforts to mitigate plastic pollution," *Science*, vol. 369, no. 6510, pp. 1515–1518, 2020.

[2] L. J. J. Meijer, T. van Emmerik, R. van der Ent, C. Schmidt, and L. Lebreton, "More than 1000 rivers account for 80% of global riverine plastic emissions into the ocean," *Science Advances*, vol. 7, no. 18, p. eaaz5803, 2021.

[3] N. Maximenko, J. Arvesen, G. Asner, J. Carlton, M. Castrence, L. Centurioni, Y. Chao, J. Chapman, V. Chirayath, and P. Corradi, "Remote sensing of marine debris to study dynamics, balances and trends," *White Paper, Decadal Survey for Earth Science and Applications from Space*, vol. 22, 2016.

[4] T. van Emmerik, T.-C. Kieu-Le, M. Loozen, K. van Oeveren, E. Strady, X.-T. Bui, M. Egger, J. Gasperi, L. Lebreton, P.-D. Nguyen, A. Schwarz, B. Slat, and B. Tassin, "A Methodology to Characterize Riverine Macroplastic Emission Into the Ocean," *Frontiers in Marine Science*, vol. 5, no. 372, 2018. [Online]. Available: https://www.frontiersin.org/article/10.3389/fmars.2018.00372

[5] P. Tasseron, T. van Emmerik, J. Peller, L. Schreyers, and L. Biermann, "Advancing Floating Macroplastic Detection from Space Using Experimental Hyperspectral Imagery," *Remote Sensing*, vol. 13, no. 12, p. 2335, 2021. [Online]. Available: https://www.mdpi.com/2072-4292/13/12/2335

[6] S. P. Garaba, T. Acuña-Ruz, and C. B. Mattar, "Hyperspectral longwave infrared reflectance spectra of naturally dried algae, anthropogenic plastics, sands and shells,"

Earth Syst. Sci. Data, vol. 12, no. 4, pp. 2665–2678, 2020. [Online]. Available: https://essd.copernicus.org/articles/12/2665/2020/

[7] M. Mehrubeoglu, A. Van Sickle, and L. McLauchlan, "Borrowing least squares analysis from spectral unmixing to classify plastics in SWIR hyperspectral images," in *Hyperspectral Imaging and Applications*, vol. 11576. International Society for Optics and Photonics, 2020, p. 115760B.

[8] G. Bonifazi, G. Capobianco, and S. Serranti, "A hierarchical classification approach for recognition of low-density (LDPE) and high-density polyethylene (HDPE) in mixed plastic waste based on short-wave infrared (SWIR) hyperspectral imaging," *Spectrochimica Acta Part A: Molecular and Biomolecular Spectroscopy*, vol. 198, pp. 115–122, 2018. [Online]. Available: http://www.sciencedirect.com/science/article/pii/S1386142518301975

[9] M. Moroni, A. Mei, A. Leonardi, E. Lupo, and F. L. Marca, "PET and PVC Separation with Hyperspectral Imagery," *Sensors*, vol. 15, no. 1, pp. 2205–2227, 2015. [Online]. Available: https://www.mdpi.com/1424-8220/15/1/2205

[10] M. Moroni and A. Mei, "Characterization and Separation of Traditional and Bio-Plastics by Hyperspectral Devices," *Applied Sciences*, vol. 10, no. 8, 2020.

[11] L. Goddijn-Murphy and J. Dufaur, "Proof of concept for a model of light reflectance of plastics floating on natural waters," *Marine Pollution Bulletin*, vol. 135, pp. 1145–1157, 2018. [Online]. Available: http://www.sciencedirect.com/science/article/pii/S0025326X18306088

[12] T. M. Karlsson, H. Grahn, B. van Bavel, and P. Geladi, "Hyperspectral imaging and data analysis for detecting and determining plastic contamination in seawater filtrates," *Journal of near infrared spectroscopy*, vol. 24, no. 2, pp. 141–149, 2016.

[13] L. Corbari, A. Maltese, F. Capodici, M. C. Mangano, G. Sarà, and G. Ciraolo, "Indoor spectroradiometric characterization of plastic litters commonly polluting the Mediterranean Sea: toward the application of multispectral imagery," *Scientific Reports*, vol. 10, no. 1, pp. 1–12, 2020.

[14] S. P. Garaba, M. Arias, P. Corradi, T. Harmel, R. de Vries, and L. Lebreton, "Concentration, anisotropic and apparent colour effects on optical reflectance properties of virgin and ocean-harvested plastics," *Journal of Hazardous Materials*, vol. 406, p. 124290, 2021.

[15] S. P. Garaba and H. M. Dierssen, "Hyperspectral ultraviolet to shortwave infrared characteristics of marine-harvested, washed-ashore and virgin plastics," *Earth System Science Data*, vol. 12, no. 1, pp. 77–86, 2020.

[16] E. Knaeps, S. Sterckx, G. Strackx, J. Mijnendonckx, M. Moshtaghi, S. P. Garaba, and D. Meire, "Hyperspectral-reflectance dataset of dry, wet and submerged marine litter," *Earth System Science Data*, vol. 13, no. 2, pp. 713–730, 2021.

[17] S. Serranti, R. Palmieri, G. Bonifazi, and A. Cózar, "Characterization of microplastic litter from oceans by an innovative approach based on hyperspectral imaging," *Waste Management*, vol. 76, pp. 117–125, 2018. [Online]. Available: https://www.sciencedirect.com/science/article/pii/S0956053X18301466

[18] M. Moshtaghi, E. Knaeps, S. Sterckx, S. Garaba, and D. Meire, "Spectral reflectance of marine macroplastics in the VNIR and SWIR measured in a controlled environment," *Scientific Reports*, vol. 11, no. 1, pp. 1–12, 2021.

[19] S. P. Garaba, J. Aitken, B. Slat, H. M. Dierssen, L. Lebreton, O. Zielinski, and J. Reisser, "Sensing Ocean Plastics with an Airborne Hyperspectral Shortwave Infrared Imager," *Environmental Science & Technology*, vol. 52, no. 20, pp. 11 699–11 707, 2018. [Online]. Available: https://doi.org/10.1021/acs.est.8b02855

[20] M. Balsi, M. Moroni, V. Chiarabini, and G. Tanda, "High-Resolution Aerial Detection of Marine Plastic Litter by Hyperspectral Sensing," *Remote Sensing*, vol. 13, no. 8, p. 1557, 2021.

[21] J. Cocking, B. E. Narayanaswamy, C. M. Waluda, and B. J. Williamson, "Aerial detection of beached marine plastic using a novel, hyperspectral short-wave infrared (SWIR) camera," *ICES Journal of Marine Science*, 2022. [Online]. Available: https://doi.org/10.1093/icesjms/fsac006

[22] V. Martínez-Vicente, J. R. Clark, P. Corradi, S. Aliani, M. Arias, M. Bochow, G. Bonnery, M. Cole, A. Cózar, R. Donnelly, F. Echevarría, F. Galgani, S. P. Garaba, L. Goddijn-Murphy, L. Lebreton, H. A. Leslie, P. K. Lindeque, N. Maximenko, F.-R. Martin-Lauzer, D. Moller, P. Murphy, L. Palombi, V. Raimondi, J. Reisser, L. Romero, S. G. H. Simis, S. Sterckx, R. C. Thompson, K. N. Topouzelis, E. van Sebille, J. M. Veiga, and A. D. Vethaak, "Measuring Marine Plastic Debris from Space: Initial Assessment of Observation Requirements," *Remote Sensing*, vol. 11, no. 20, 2019.

[23] H. Huang, J. U. Qureshi, S. Liu, Z. Sun, C. Zhang, and H. Wang, "Hyperspectral imaging as a potential online detection method of microplastics," *Bulletin of Environmental Contamination and Toxicology*, vol. 107, no. 4, pp. 754–763, 2021.

[24] H. J. Reinders and A. M. Land-Zandstra, "Citizen Science voor Schone Rivieren."

[25] C. van Lieshout, K. van Oeveren, T. van Emmerik, and E. Postma, "Automated River Plastic Monitoring Using Deep Learning and Cameras," *Earth and Space Science*, vol. 7, no. 8, p. e2019EA000960, 2020. [Online]. Available: https://doi.org/10.1029/2019EA000960

[26] T. van Emmerik and S. de Lange, "Pilot monitoring drijvend zwerfafval en macroplastics in rivieren: jaarmeting 2021," Tech. Rep., 2022.

[27] P. Tasseron, T. van Emmerik, L. Schreyers, L. Biermann, and J. Peller, "Hyperspectral plastics dataset supplementary to the paper 'Advancing floating plastic detection from space using hyperspectral imagery'," 4 2021. [Online]. Available: 10.4121/14518278

[28] M. C. C. De Graaf, H. M. Van de Steeg, L. Voesenek, and C. Blom, *Vegetatie in de uiterwaarden: de invloed van hydrologie, beheer en substraat.* KU, 1990.

[29] Z. Ren, L. Sun, and Q. Zhai, "Improved k-means and spectral matching for hyperspectral mineral mapping," *International Journal of Applied Earth Observation and Geoinformation*, vol. 91, p. 102154, 2020. [Online]. Available: https://www.sciencedirect.com/science/article/pii/S0303243420300714

[30] S. L. Al-Khafaji, J. Zhou, A. Zia, and A. W.-C. Liew, "Spectral-spatial scale invariant feature transform for hyperspectral images," *IEEE Transactions on Image Processing*, vol. 27, no. 2, pp. 837–850, 2017.

[31] P. Kumar, D. K. Gupta, V. N. Mishra, and R. Prasad, "Comparison of support vector machine, artificial neural network, and spectral angle mapper algorithms for crop classification using LISS IV data," *International Journal of Remote Sensing*, vol. 36, no. 6, pp. 1604–1617, 2015.

[32] G. Gopinath, N. Sasidharan, and U. Surendran, "Landuse classification of hyperspectral data by spectral angle mapper and support vector machine in humid tropical region of India," *Earth Science Informatics*, vol. 13, no. 3, pp. 633–640, 2020.

[33] V. Van Belle, K. Pelckmans, S. Van Huffel, and J. A. K. Suykens, "Improved performance on high-dimensional survival data by application of Survival-SVM," *Bioinformatics*, vol. 27, no. 1, pp. 87–94, 2011.

[34] P. C. Deka, "Support vector machine applications in the field of hydrology: a review," *Applied soft computing*, vol. 19, pp. 372–386, 2014.

[35] Y. Chen, L. Zhu, P. Ghamisi, X. Jia, G. Li, and L. Tang, "Hyperspectral images classification with Gabor filtering and convolutional neural network," *IEEE Geoscience and Remote Sensing Letters*, vol. 14, no. 12, pp. 2355–2359, 2017.

[36] X. Ying, "An overview of overfitting and its solutions," in *Journal of Physics: Conference Series*, vol. 1168, no. 2. IOP Publishing, 2019, p. 22022.

[37] G. P. Petropoulos, K. P. Vadrevu, G. Xanthopoulos, G. Karantounias, and M. Scholze, "A comparison of spectral angle mapper and artificial neural network classifiers combined with Landsat TM imagery analysis for obtaining burnt area mapping," *Sensors*, vol. 10, no. 3, pp. 1967–1985, 2010.

[38] G. Girouard, A. Bannari, A. El Harti, and A. Desrochers, "Validated spectral angle mapper algorithm for geological mapping: comparative study between QuickBird and Landsat-TM," in *XXth ISPRS congress, geo-imagery bridging continents, Istanbul, Turkey*, 2004, pp. 12–23.

[39] A. A. Lacis and J. Hansen, "A parameterization for the absorption of solar radiation in the earth's atmosphere," *Journal of Atmospheric Sciences*, vol. 31, no. 1, pp. 118–133, 1974.

[40] H. C. Hottel, "A simple model for estimating the transmittance of direct solar radiation through clear atmospheres," *Solar Energy*, vol. 18, no. 2, pp. 129–134, 1976. [Online]. Available: https://www.sciencedirect.com/science/article/pii/0038092X76900451

[41] F. M. Danson, M. D. Steven, T. J. Malthus, and J. A. Clark, "High-spectral resolution data for determining leaf water content," *International Journal of Remote Sensing*, vol. 13, no. 3, pp. 461–470, 1992.

[42] T. van Emmerik, C. T. J. Roebroek, W. de Winter, P. Vriend, M. Boonstra, and M. Hougee, "Riverbank macrolitter in the Dutch Rhine-Meuse delta," *Environmental Research Letters*, 2020.

[43] R. J. Murphy, S. T. Monteiro, and S. Schneider, "Evaluating classification techniques for mapping vertical geology using field-based hyperspectral sensors," *IEEE Transactions on Geoscience and Remote Sensing*, vol. 50, no. 8, pp. 3066–3080, 2012.

[44] M. B. Stuart, A. J. S. McGonigle, and J. R. Willmott, "Hyperspectral Imaging in Environmental Monitoring: A Review of Recent Developments and Technological Advances in Compact Field Deployable Systems," *Sensors*, vol. 19, no. 14, p. 3071, 2019. [Online]. Available: https://www.mdpi.com/1424-8220/19/14/3071

[45] T. Adão, J. Hruška, L. Pádua, J. Bessa, E. Peres, R. Morais, and J. J. Sousa, "Hyperspectral imaging: A review on UAV-based sensors, data processing and applications for agriculture and forestry," *Remote Sensing*, vol. 9, no. 11, p. 1110, 2017.

[46] T. C. Wilkes, T. D. Pering, A. J. S. McGonigle, G. Tamburello, and J. R. Willmott, "A low-cost smartphone sensor-based UV camera for volcanic SO2 emission measurements," *Remote Sensing*, vol. 9, no. 1, p. 27, 2017.

[47] C. C. Wilcox, M. Montes, M. Yetzbacher, J. Edelberg, and J. Schlupf, "An ultra-compact hyperspectral imaging system for use with an unmanned aerial vehicle with smartphone-sensor technology," in *Micro-and Nanotechnology Sensors, Systems, and Applications X*, vol. 10639. International Society for Optics and Photonics, 2018, p. 1063919.

[48] R. A. Borsoi, T. Imbiriba, J. C. M. Bermudez, C. Richard, J. Chanussot, L. Drumetz, J.-Y. Tourneret, A. Zare, and C. Jutten, "Spectral variability in hyperspectral data unmixing: A comprehensive review," *arXiv preprint arXiv:2001.07307*, 2020.

[49] X. Li, J. Xiao, J. B. Fisher, and D. D. Baldocchi, “ECOSTRESS estimates gross primary production with fine spatial resolution for different times of day from the International Space Station,” *Remote sensing of environment*, vol. 258, p. 112360, 2021.

[50] J. Cardoso-Fernandes, J. Silva, A. Lima, A. C. Teodoro, M. Perrotta, J. Cauzid, and E. Roda-Robles, “Characterization of lithium (Li) minerals from the Fregeneda-Almendra region through laboratory spectral measurements: a comparative study,” in *Earth Resources and Environmental Remote Sensing/GIS Applications XI*, vol. 11534. International Society for Optics and Photonics, 2020, p. 115340N.

[51] C.-C. Chang and C.-J. Lin, “LIBSVM: a library for support vector machines,” *ACM transactions on intelligent systems and technology (TIST)*, vol. 2, no. 3, pp. 1–27, 2011.

[52] Y. Liu and Y. F. Zheng, “One-against-all multi-class SVM classification using reliability measures,” in *Proceedings. 2005 IEEE International Joint Conference on Neural Networks, 2005.*, vol. 2. IEEE, 2005, pp. 849–854.

[53] F. A. Kruse, A. B. Lefkoff, J. W. Boardman, K. B. Heidebrecht, A. T. Shapiro, P. J. Barloon, and A. F. H. Goetz, “The spectral image processing system (SIPS)—interactive visualization and analysis of imaging spectrometer data,” *Remote sensing of environment*, vol. 44, no. 2-3, pp. 145–163, 1993.

[54] I. C. Chein, “An information-theoretic approach to spectral variability, similarity, and discrimination for hyperspectral image analysis,” *IEEE Transactions on Information Theory*, vol. 46, no. 5, pp. 1927–1932, 2000.

[55] ——, “Spectral information divergence for hyperspectral image analysis,” in *IEEE 1999 International Geoscience and Remote Sensing Symposium. IGARSS’99 (Cat. No.99CH36293)*, vol. 1, 1999, pp. 509–511.

[56] M. Khaleghi, H. Ranjbar, J. Shahabpour, and M. Honarmand, “Spectral angle mapping, spectral information divergence, and principal component analysis of the ASTER SWIR data for exploration of porphyry copper mineralization in the Sarduiyeh area, Kerman province, Iran,” *Applied Geomatics*, vol. 6, no. 1, pp. 49–58, 2014.

[57] Y. Du, C.-I. Chang, H. Ren, C.-C. Chang, J. O. Jensen, and F. M. D’Amico, “New hyperspectral discrimination measure for spectral characterization,” *Optical Engineering*, vol. 43, no. 8, pp. 1777–1786, 2004.